FY20 Los Alamos National Laboratory Experimental Campaigns at the Omega Laser Facility

P. A. Keiter, E. Loomis, S. Palaniyappan, B. Scheiner, A. Rasmus, H. Johns, K. Flippo, and Y. Kim

Los Alamos National Laboratory

Evaluating the Shock Behavior of Be to W Metal Gradient Foils on OMEGA EP

Principal Investigators: E. Loomis, D. Stark, A. Strickland, S. Palaniyappan, P. A. Keiter, T. Cardenas, and J. Sauppe (LANL); and M. Huff[*] (Dept. of Physics & Astronomy, University of Rochester)
[*]Also LLE

Los Alamos National Laboratory (LANL) is currently assessing double-shell implosions as a potential platform for reaching volumetric thermonuclear burn at the National Ignition Facility (NIF). In double-shell capsules, an outer low-Z ablator is accelerated inward with x rays or lasers toward a high-Z, dense inner shell containing liquid-fill DT fuel. One of the major sources of degradation in these capsules is the growth of hydrodynamic instabilities on the surface of the high-Z shell. One mitigation strategy for controlling this instability growth is the use of a graded-density shell between the high-density metal and a lower-density metal, which provides a gradient scale length to suppress instability growth during shell collision. Our current design uses tungsten graded into beryllium; however, when shocked to hundreds of Mbar, the behavior of this graded-density and composition material is unknown.

We are therefore studying the planar behavior of graded metal targets on OMEGA and OMEGA EP. During our first shot day in FY20 we studied the 1-D shock compression of Be/W graded targets on OMEGA EP. These experiments used a similar target design as that described in Ref. 1; our target design is detailed in Fig. 1(a). Here, a bilayer target was placed side-by-side with a
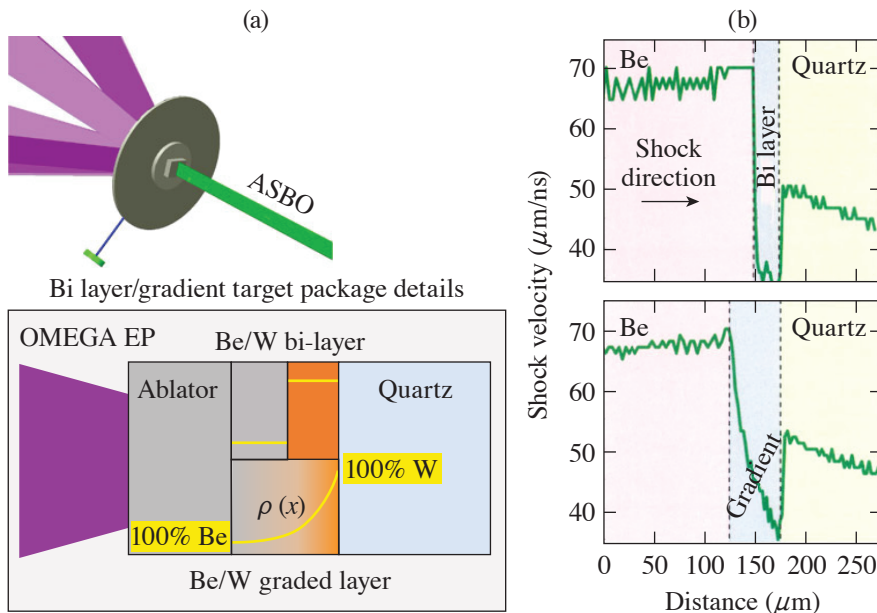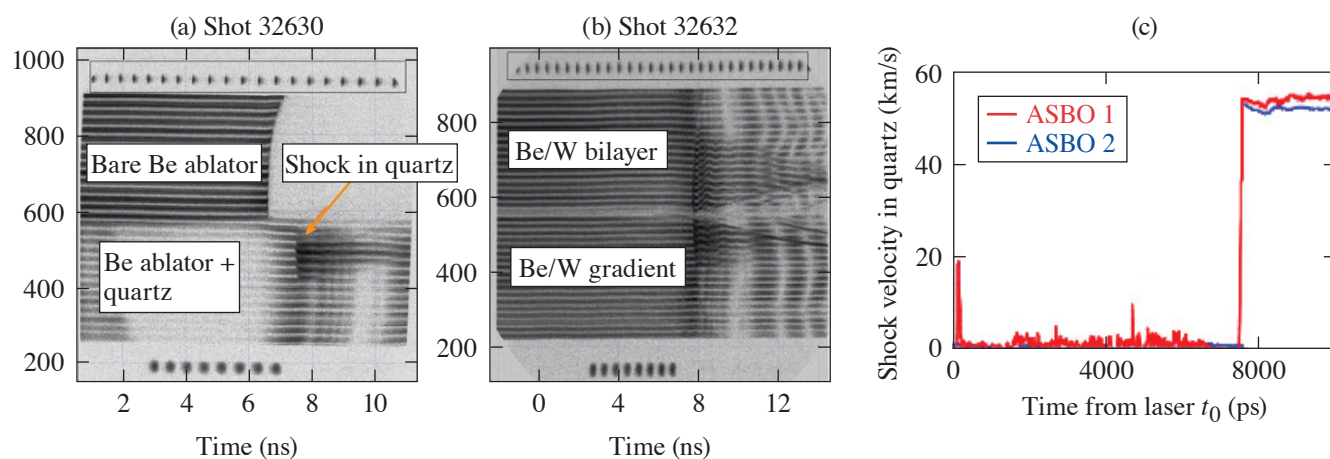

Figure 1

(a) Planar DSMATGRAD target driven by four OMEGA EP long-pulse beams of 6-ns duration. Details of the target include Be ablator, side-by-side Be/W bilayer and gradient-layer specimens, and quartz window for shock-wave measurement using the ASBO diagnostic. (b) LANL *xRAGE* simulations show the difference in shock velocity through the bilayer versus the gradient-layer sample.

U2628JR

gradient-layer target on a Be ablator. Placed on the high-Z side of both the bilayer and gradient layer was a quartz window that allowed us to view the shock front directly with the active shock breakout (ASBO) diagnostic. Simulations of both the bilayer and graded layer using the LANL *xRAGE* code are shown in Fig. 1(b), where a decelerating shock is seen as the shock propagates up the density gradient. This is starkly different from the bilayer target, where a simple discrete jump occurs at the sharp Be/W interface.

Figure 2 shows representative data from the DSMATGRAD-EP shot day where on shot 32630 we removed the bilayer and gradient-layer targets to simply have a quartz window against the Be ablator. This was done to characterize the ablator drive prior to entering the metal specimens. Here we measured a shock velocity entering the quartz from the ablator of 55 km/s [Fig. 2(b)]. In shot 32632 we used a bilayer/gradient-layer target that was roughly 30 μm thick. The ASBO image in Fig. 2(c) shows fringe motion on both the bilayer and gradient-layer sides. The data analysis is still in progress for this shot, but the fringe motion does appear to be different in the bilayer side relative to the gradient side.

Figure 2

ASBO interferometry data from two shots. (a) Data from the Be ablator/quartz target from shot 32630 where the shock becomes reflecting inside the quartz window and (b) the measured shock velocity entering the quartz from the ablator of 55 km/s; (c) Shot 32632, which used a bilayer/gradient-layer target. Differences in fringe motion (and shock velocity) are seen on either side of the Be/W target once the shock enters the quartz.

Laser-Driven X-Ray Radiography of Shocked Chromium Foils
Principal Investigators: S. Palaniyappan, D. Broughton, C. Huang, A. Favalli, M. Iliev, A. Junghans, P. Singh, and R. Reinovsky (LANL); N. Lemos, A. Mckinnon, and A. Pak (LLNL); and S. Klein (University of Michigan)

1. Multi-Probe 20A (13 February 2020)
    The experimental setup for radiographing static objects on OMEGA EP is shown in Fig. 3. A 50-J (2-ps) laser pulse, called a "sidelighter," impinges on a 0.5-mm^3 tantalum cube from the left. The tantalum cube is held by the Target Positioning System (TPS-7). The laser interacts with the front surface of the tantalum cube and drives an intense multi-MeV electron beam along the direction of the laser beam. The rest of the tantalum cube acts as a converter and generates x rays via bremsstrahlung. A filter stack spectrometer sitting nearly perpendicular to the laser beam is used to measure the x-ray spectrum. The tantalum cube stops electrons up to an energy of 1 MeV, and electrons with higher energies lose some of their energy as they transmit through the converter. The transmitted electrons can contribute to a large background signal on the image-plate (IP) detector. To partially mitigate this issue, a 2-mm-thick aluminum block was placed 5 mm away from the tantalum cube to block some of the high-energy electrons. The x rays transmit through the physics package and are then recorded using an IP stack. The IP stack has five IP's (each 2 ft $\times$ 2 ft square) with copper filters of varying thickness sandwiched in between.

Figure 4 shows the x-ray spectrum measured using the filter stack x-ray spectrometer. The first image plate on the IP stack has a 200-mm-thick copper filter, while the subsequent IP's had a 50-μm-thick copper filter. In this setup, the image plates were seeing the x ray with energies 35 keV and above.

Figure 5(a) above shows a sketch of the static layers that were radiographed [Fig. 5 (b)] with laser-driven x rays. The static object contained three layers: a 500-μm-thick CH foil, a 100-μm-thick tantalum foil, and a 500-μm-thick chromium foil stacked together. In the x-ray line of sight, these layers were 2 mm long. The x-ray radiographs were taken at x-ray energies of 30 keV and
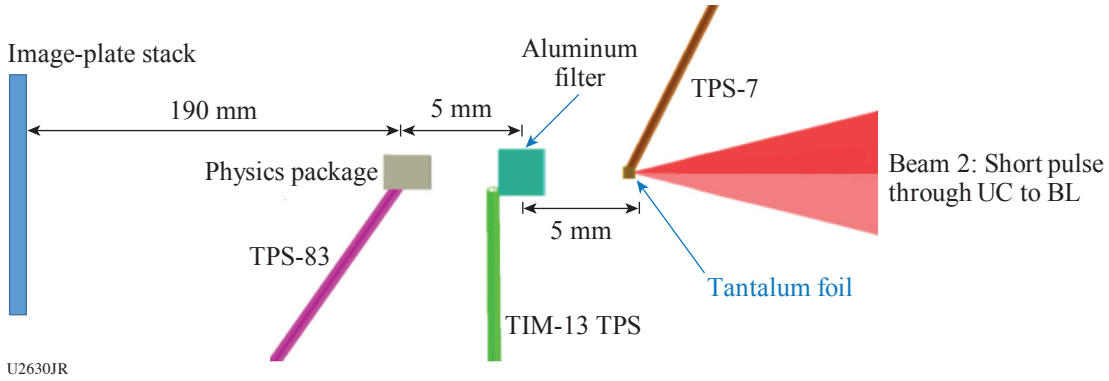

U2630JR

Figure 3
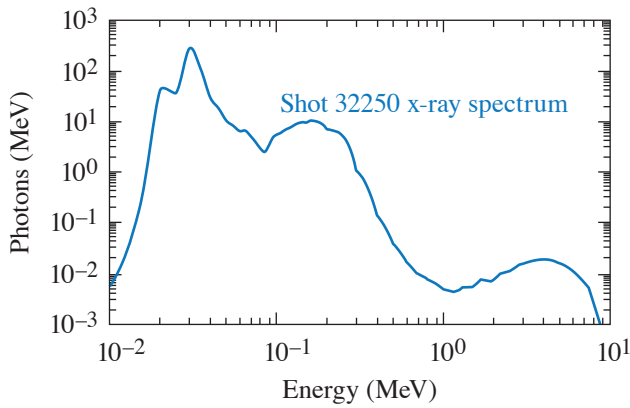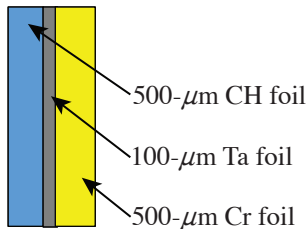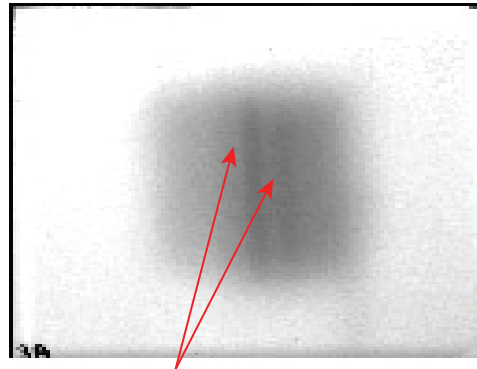Experimental setup on the OMEGA EP laser for static radiography.

U2631JR

Figure 4
Measured x-ray spectrum for a typical shot (32250).

U2632JR

Figure 5
X-ray radiograph of static layers.

above. The x-ray radiograph [Fig. 5 (b)] shows a dual image of the tantalum layer. We believe that the dual x-ray source most likely comes from the driving laser filamenting in the pre-plasma in front of the tantalum target with which the short-pulse laser interacts.

Figure 6 shows the x-ray radiograph of a chromium foil that was driven by three long-pulse laser beams (4.5 KJ each, 10 ns long) that were stacked in a line to create a 1.5-mm long line focus onto the chromium foil. The shocked chromium was expected to double its density. This would lead to shocked chromium with an areal density of 1.1 g/cm^2. It is very unlikely that the darker region in Fig. 6 is the shocked chromium because we do not see the edges of the chromium foil. At the end of this campaign, we identified several issues that prevented us from obtaining a high-resolution and high-quality radiograph: (1) We observed a dual x-ray source that most likely came from laser filamentation on the front side of the tantalum foil interacting with the short-pulse laser. (2) We observed relatively high background counts of ~30 K on the image-plate detector. This background was the same whether the long-pulse beam was on or off. This implied that the background signal on the image plate was due to the short pulse. We suspect it was mostly the electrons that were not stopped within the tantalum converter impinging on the image plate. (3) We also noticed that some stray x-ray light was coming into the image-plate pack from the side.
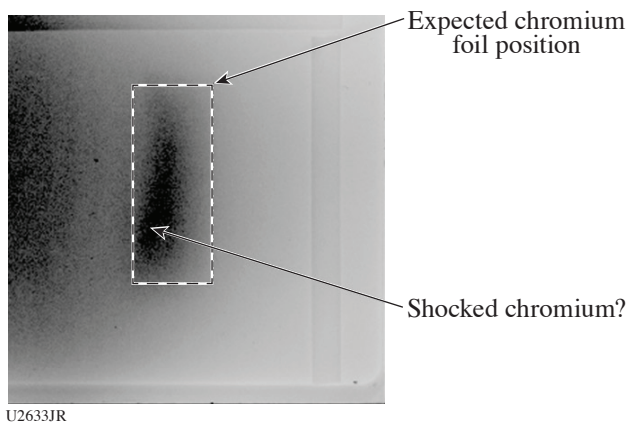

Expected chromium foil position

Shocked chromium?

U2633JR

Figure 6
X-ray radiograph of the chromium foil driven by three long-pulse beams.

2. Multi-Probe 20B (3 September 2020)

During the first campaign of the experiment, we realized that several issues were preventing us from getting a good x-ray radiograph (as was discussed above). For the second experimental campaign, several improvements were made to mitigate the issues that were present during the first shot day.

Figure 7 shows the improved experimental setup for the second shot day. The improvements included using a compound parabolic concentrator (CPC) cone with a tantalum wire, using a magneto-inertial fusion electrical discharge system (MIFEDS) magnetic-field coil, and covering the sides of the image-plate pack with 500-μm-thick copper.

TIM-13 TPS

MIFEDS

Sidelighter

Beam 1: Short pulse through LC to SL

TPS-7

CPC cone/ Ta wire

Physics package
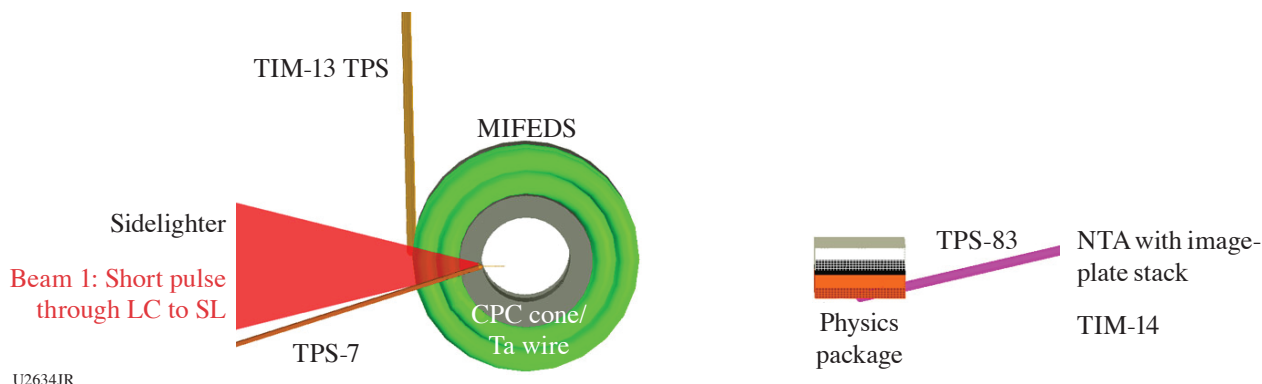
TPS-83

NTA with image-plate stack

TIM-14

U2634JR

Figure 7
Experimental setup for the second shot day. NTA: near-target arm.

3. Compound Parabolic Concentrator

A sketch of the CPC is shown in Fig. 8(a).[2] The parabolic surface of the CPC ensures that rays coming in with an incident angle less than a certain value are focused at the tip of the cone. Figure 8(c) shows a 3-D–printed CPC cone with a handling tab that we used in the OMEGA EP experiment pictured on a grain of rice. The CPC cone focuses the laser beam to a single focal spot at the tip of the cone.
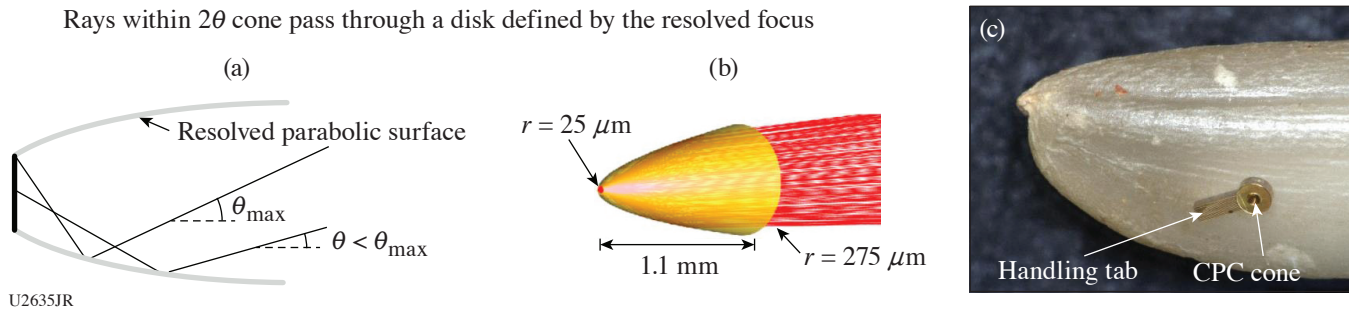
Rays within 2θ cone pass through a disk defined by the resolved focus

(a) (b)

Resolved parabolic surface

θ_{max}

$\theta < \theta_{max}$

U2635JR

$r = 25\ \mu m$

1.1 mm $r = 275\ \mu m$

(c)

Handling tab   CPC cone

Figure 8
(a) A sketch of the CPC, (b) a CAD model of a CPC cone, and (c) an actual 3-D–printed CPC cone with a handling tab on a grain of rice that we used in our OMEGA EP experiment.

A 25-μm-thick, 500-μm-long tantalum wire is attached at the tip of the CPC cone as shown in Fig. 9. The CPC cone/wire combination ensures that we get a single source of x rays. This setup is also expected to provide x rays with a source size of the order of the wire thickness for high-resolution radiography.
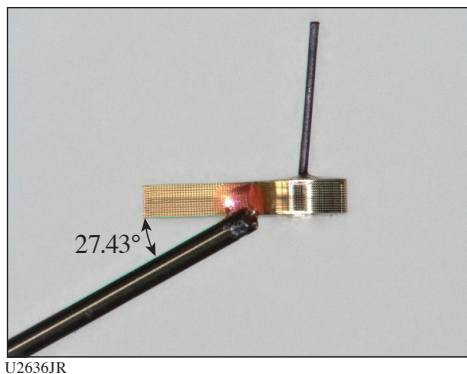
27.43°

U2636JR

Figure 9
CPC cone with a tantalum wire attached to the cone tip.

Figure 10 shows the expected field distribution from the 50-T MIFEDS coil used in our experiment.[3] The center of the coil was placed 2 mm away from the target chamber center (TCC), where we still expect magnetic fields strong enough to deflect the electrons escaping the tantalum wire away from the IP pack detector, thereby significantly reducing the background count.

Figure 11 shows the 500-μm-thick copper plate, shaped like a box lid, in which the IP pack sits. This prevents any stray light from entering the IP pack from the side and increasing the background on the IP. The improvements (CPC cone/wire, MIFEDS coil, and the IP pack cover) are expected to mitigate the issues we experienced in the first shot day that prevented us from getting high-resolution and high-quality radiographs.

Figure 12 shows static x-ray radiographs of the CH/Ta/Cr layers. The plastic layer is not visible in the radiograph. The fourth and fifth layers had 350 μm and 400 μm of copper in front of them, respectively. With these filters, the image plates see x rays above 35 keV. The x-ray radiograph from shot 32254 had an edge blur of ~40 μm, which is of the order of the wire thickness. In
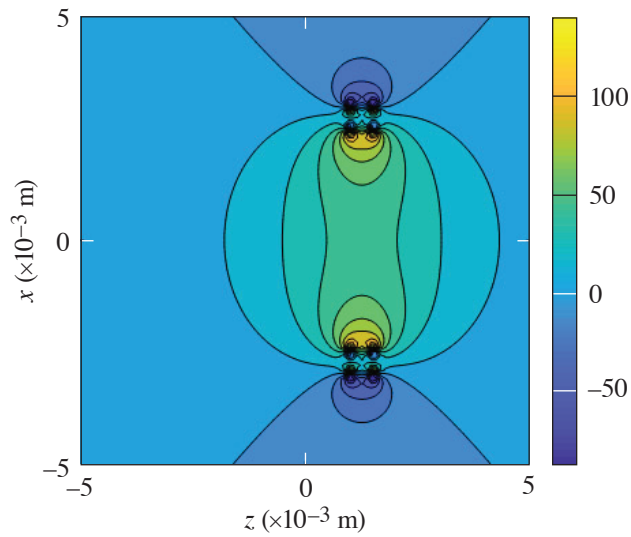
Figure 10
Magnetic-field distribution from a 50-T MIFEDS coil.

U2637JR

Figure 11
A 500-μm-thick copper dip that covers the sides of the IP pack, except the front, to help reduce the background on the IP.

U2638JR

(a) Static physics package

100-μm Ta foil

500-μm CH foil → ← 500-μm Cr foil

U2639JR

(b) X-ray static image shot 32251
(fourth layer)

Ta foil   Cr foil

(c) X-ray static image shot 32254
(fifth layer)

Ta foil   Cr foil
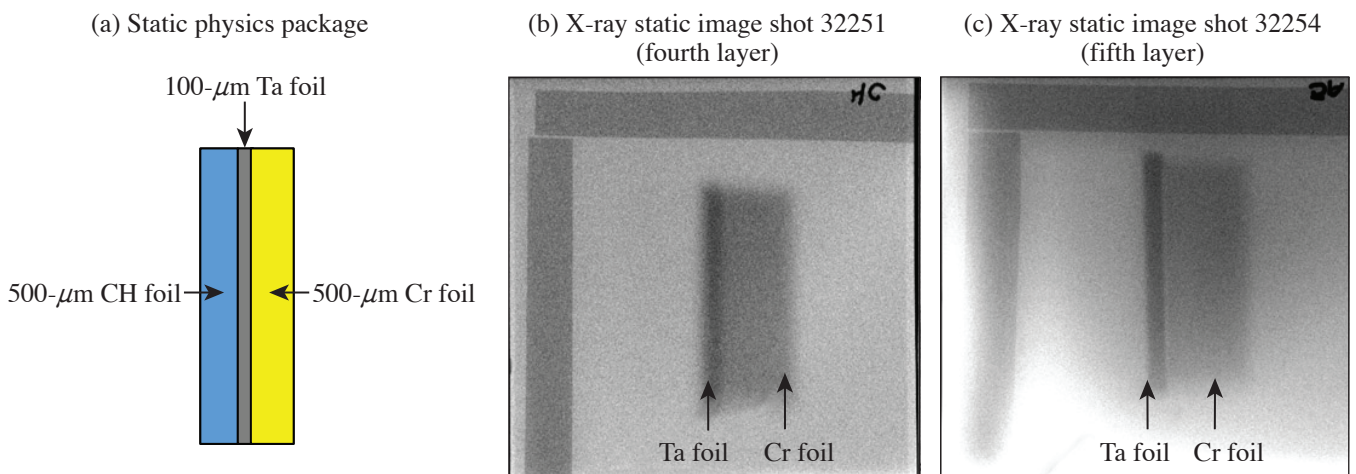
Figure 12
Static x-ray radiograph of the CH/Ta/Cr layers stack.

comparison, shot 32251 had a larger edge blur. We believe this difference is associated with variation in the intensity on the Ta wire due to variation from the focusing capability of the CPC cone. We are still trying to understand this effect.

Table I lists the shots and the corresponding laser parameters used on the second shot day.

Table I: Shots performed with the parameters.

Number	Shot #	SRF	Short-pulse energy	Short-pulse duration	Short-pulse turn on (ns)	Long-pulse beams on/off	Long-pulse turn on (ns)	Total delay (ns)	Static/ Dynamic
1	33250	78050	200 J	5 ps	0	Off			Static
2	33252	79156	50 J	5 ps	0	Off			Static
3	33253	79157	20 J	10 ps	0	Off			Static
4	33254	79158	20 J	5 ps	0	Off			Static
5	33255	78051	20 J	5 ps	16	On	0	16	Dynamic
6	33256	79161	20 J	5 ps	16	On	−10	26	Dynamic

Figure 13 shows the dynamic radiography of the chromium foil that was shocked by the three long-pulse beams stacked to focus as a line. The position of the shock is consistent with the *HELIOS* 1-D radiation-hydrodynamic predictions. We see that the x-ray source size is larger in these radiographs. We are still trying to understand this effect as we discussed above.
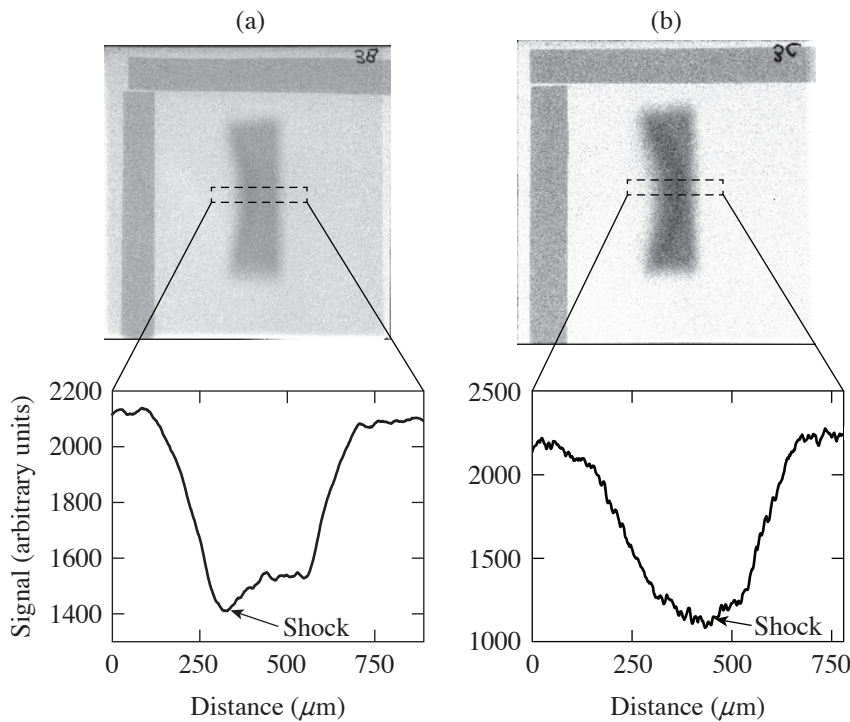

Figure 13

X-ray radiograph of shocked chromium foil at 16 ns (shot 32255) and 26 ns (shot 32256).

U2640JR

Radishock 2020 Annual Report on OMEGA

Principal Investigators: H. M. Johns, P. Kozlowski, S. Wood, H. Robey, C. Fryer, A. Liao, T. S. Perry, C. J. Fontes, J. Cowan, T. Urbatsch, and M. Douglas (LANL); and J. W. Morton and C. R. D. Brown (AWE)

The Radishock experiment uses point-projection backlighting for both radiography and spectroscopy, as shown in Fig. 14. The Kr-filled capsule generates 4- to 5.5-keV photons that are absorbed by L-shell Ti ions in the driven Radishock target. These
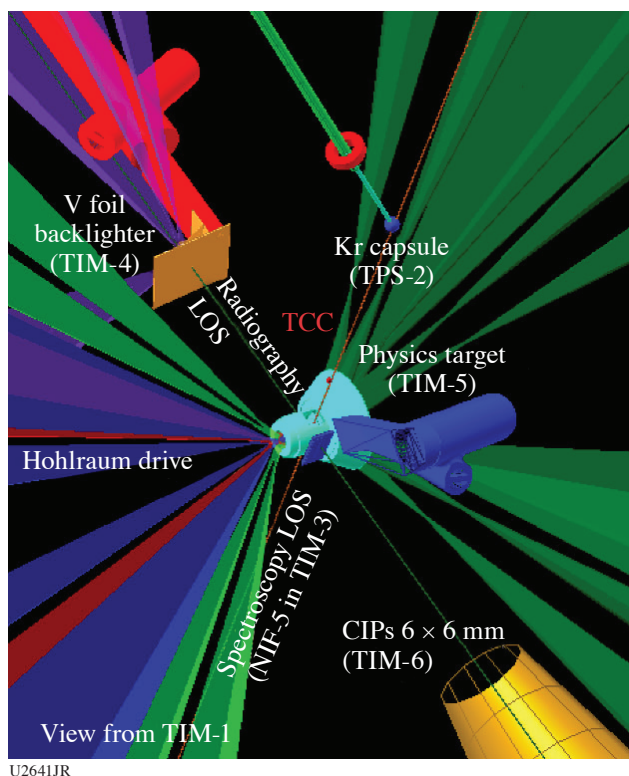
Figure 14
VisRad model for the Radishock experiment.

spectra are measured by a 1-D space-resolving spectrometer, giving us a spectrum that evolves with distance from the halfraum. The V-foil backlighter uses a 25-μm pinhole to backlight the target with V K lines, dominated by the V K-β line, to backlight the target for radiography using the 6×6-mm close-in ported snout (CIPS). We fielded additional diagnostics not shown in the VisRad. Dante was fielded to obtain the temperature of the halfraum drive. A 12$\times$ imager in TIM-1 (ten-inch manipulator) was used to image the imploded capsule, obtain the duration of the flash, and determine the size of the imploded capsule at that time. X-ray streak camera A was fielded in TIM-2 to verify the flash duration and ensure that each flash remained continuous and repeatable.

The last shot day for the Radishock Campaign was 12 March 2020. The motivation for Radishock is to study the interaction between a supersonic flow (driven by a halfraum) and a counter-propagating shock (driven by an ablator) in order to provide constraining data on radiation transport for radiation-hydrodynamic codes. The interaction is predicted to result in a Zel'dovich-like temperature spike when the foam warmed by the shock interacts with the higher-temperature plasma caused by the radiation flow. The Radishock-20A shot day was used to collect additional data on mid- and late-time spectra and radiography to improve quality. The original intended goal was to use lower-density foams to probe differences that would occur in the spike if the radiation flow were driven by reduced power (400 J/beam) versus nominal (500 J/beam). The lower-density foams needed for this objective were not of sufficient quality, however, so we instead built targets with higher-density foams and opted to prioritize our secondary goal of filling in our data set.

Our Radishock-20A shot day yielded very high quality radiography data, including the best first-shot radiograph collected for the campaign (Table II). We used the radiography data to obtain the position of the shock.

Table II: FY20 Radishock shot day.

Date	Shot day	Number of shots
12 March 2020	Radishock 20A	11

Figure 15 shows six radiographs from Radishock-20A. We treat the ablator start time as "0" in simulations. Radiographs taken during the Radishock interaction are on the left, ablator-only shots are in the center, and radiation flow-only shots (halfraum only) are on the right. The ablator-only shots were used to benchmark the ablator drive in simulations to assist with modeling interaction shots. The radflow-only radiographs verify that the flow remains supersonic at the time of interaction. In the data in Fig. 15, the ablator is toward the left and the halfraum is toward the right. The foam is visible in the center of the target, especially for ablator-only shots. An Al filter was placed over the halfraum edge to prevent early time emission near the re-entrant hole from contaminating the radiograph.
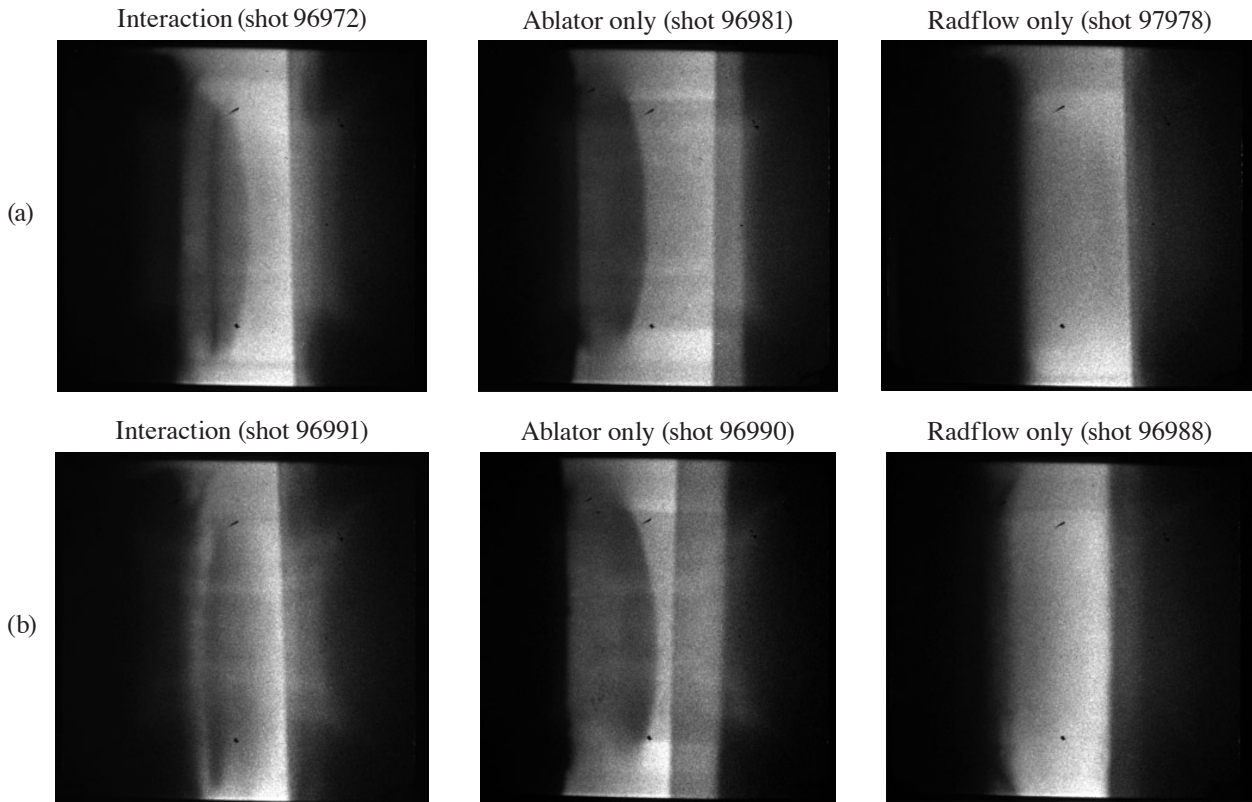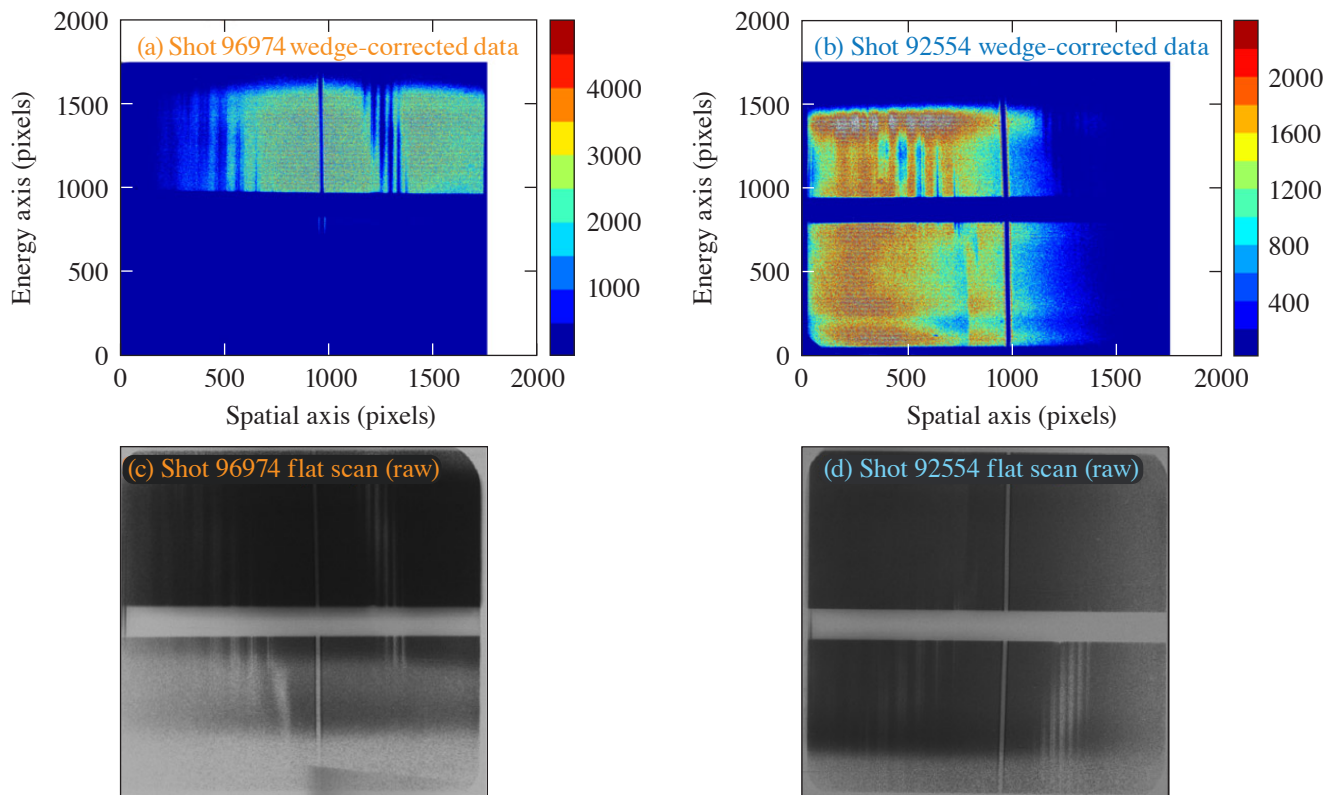

Figure 15

Radiographs from Radishock-20A: (a) 6.7 ns and (b) 8.2 ns after the ablator was fired.

Spectroscopic data collected on film in Radishock-20A were more problematic for a couple of reasons. First, issues with the timing systems in TIM-1 and TIM-3 made it difficult to both co-time the capsule flash with recording the spectroscopic data and co-time the frames for the spectroscopic data. The issue with co-timing frames had never previously occurred but occurred for essentially every shot on this particular day. An additional issue was uncovered when we worked toward processing this data: we noticed unusual features in the wedge. Figure 16 provides an example comparison between wedge-corrected data from two different shot days.

In Fig. 16(a) and (c), Frame 1 is on the bottom and Frame 2 on the top; the halfraum is on the Frame 2 side. The interaction is visible in the raw data [see Fig. 16(c)] in 20A in Frame 1, but not visible on the top. This means that for Radishock-20A, none of our interaction shots actually captured useful spectra at the location of the interaction. The reason why these data seem to be visible in the flat field is explained in Fig. 17, which compares the curves for the wedge corrections from 19A (which is fairly normal) with the unusual wedge correction we obtained for Radishock-20A. For the shot from Radishock-19A, the intensity for the continuum is largely the same for both frames, and the intensity drops in the same position (because for early times this particular shot was not aligned with the backlighter flash).

The shot from 19A in Fig. 17 has a nominal wedge correction for that day and indeed is very similar to wedges for all previous days from the Radishock Campaign. The shot (96974) selected for Radishock-20A has the same shape as the others for that

Figure 16
A comparison between [(a),(b)] wedge corrected and [(c),(d)] raw data for a shot from [(a),(c)] Radishock-20A and [(b),(d)] Radishock-19A.
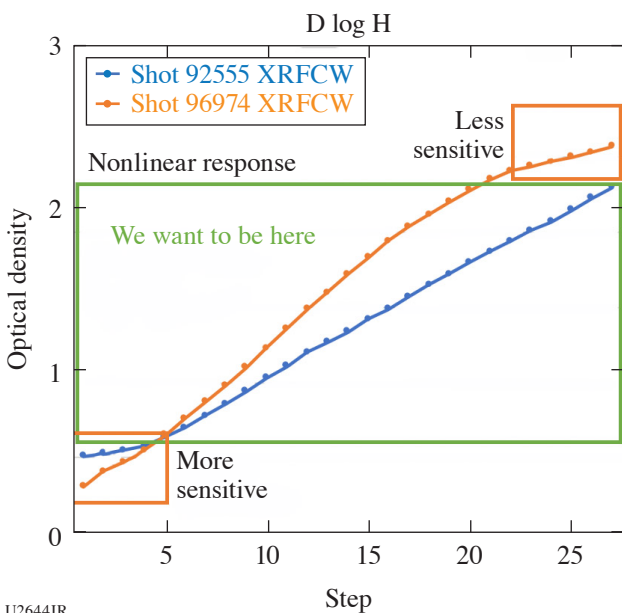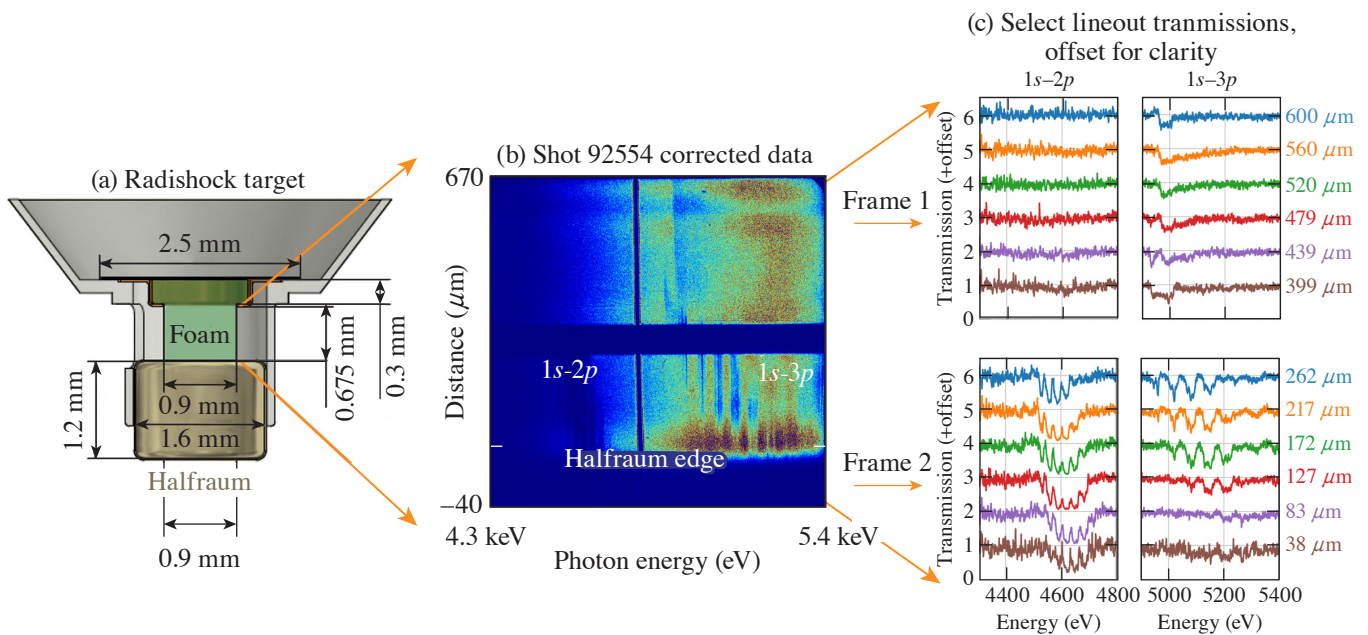

Figure 17
The wedge calibration curves for two shots from Radishock-20A (orange curve, shot 96974) and Radishock-19A (blue curve, shot 92555). This comparison was done as part of a study by J. Cowan, the resident film expert for P-24.

shot day, so it is a representative example. These calibration curves are the center points for the wedge steps. In both cases, the P-24 LANL delta wedge was used.

The 20A shot was taken with new film, so it is more sensitive at low signal. This is why the data from Frame 1 appears in the raw data, but the value is insignificant once the wedge correction is made. The film is more sensitive and will record intensity values that are much smaller than are "useful." The 19A shots were recorded with older film, which had significantly more fog. The points on the calibration curve corresponding to that increased sensitivity are in the box on the lower left, or points 1 to 5 on the 20A wedge. Additionally, the film development is overdriven (too hot or too long for the developer used), resulting in a much steeper intensity curve and a loss of sensitivity and nonlinear behavior at the top of the curve (steps 21 to 27). Unfortunately, this region of the wedge overlaps with intensities for our bright continuum (usually 20 to 24), which means that the peak signal we have in 20A is nonlinear. J. Cowan from P-24 is currently working with personnel at LLE to help investigate this issue in hopes that later campaigns do not see a recurrence.

The remainder of this report discusses an analysis of data of the Radishock Campaign that illustrates the current state of investigation of the results of this series of experiments.

Figure 18 shows example analyzed spectra from a set of ten shots that are being compared with synthetic spectra post-processed from radiation-hydrodynamic simulations[4] using a ray-trace model.[5] The data processing strategy is consistent with a recently submitted publication on COAX[5] spectra.


U2645JR

Figure 18

(a) Spectroscopic data collected from Radishock targets have been (b) corrected and (c) transmission lineouts have been extracted. Every second lineout above the halfraum edge is shown, each with an offset of 1.0 for clarity.

Figure 19 shows an example of post-shot simulations performed in *Cassio* using the as-shot laser power history and measured foam densities for each shot. The simulated shock position and shock curvature are in very reasonable agreement with the measured data for all shots simulated. Cutoff models are being augmented with laser ray tracing on halfraum models that allow one to set the actual laser beam parameters (number of beams, timing, pointing, energy, defocus, etc.). *Cassio* simulations' laser ray tracing includes cross-beam energy transfer and have no laser power multipliers and no shot-to-shot changes.
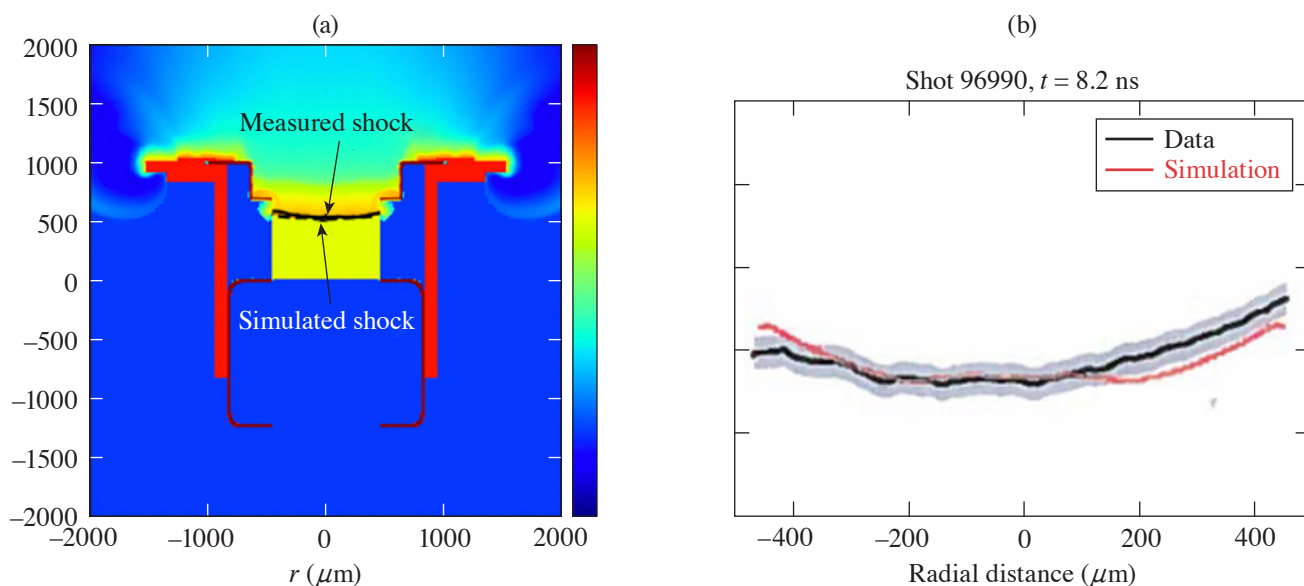
U2646JR

Figure 19
(a) Post-shot simulation of shot 96990 in (b) *Cassio*.

We have begun interrogating the processed Radishock spectra to locate the temperature spike, as seen in Fig. 20. Normally, the temperature of the radiation flow is decreased with distance from the halfraum, resulting in reduced absorption in higher-photon-energy spectral features. If instead we see a spectrum with increased absorption in these features relative to the one behind it, it means that the temperature has increased locally and we have evidence in the spectrum consistent with a temperature spike. We expect the temperature increase to be small early in time compared to later-time shots after the interaction is well established. Early uncertainty assessments imply this early-time spike is indeed measurable, but further work is needed. Figures 18–20 are intended to be part of upcoming publications to be drafted in early FY21.
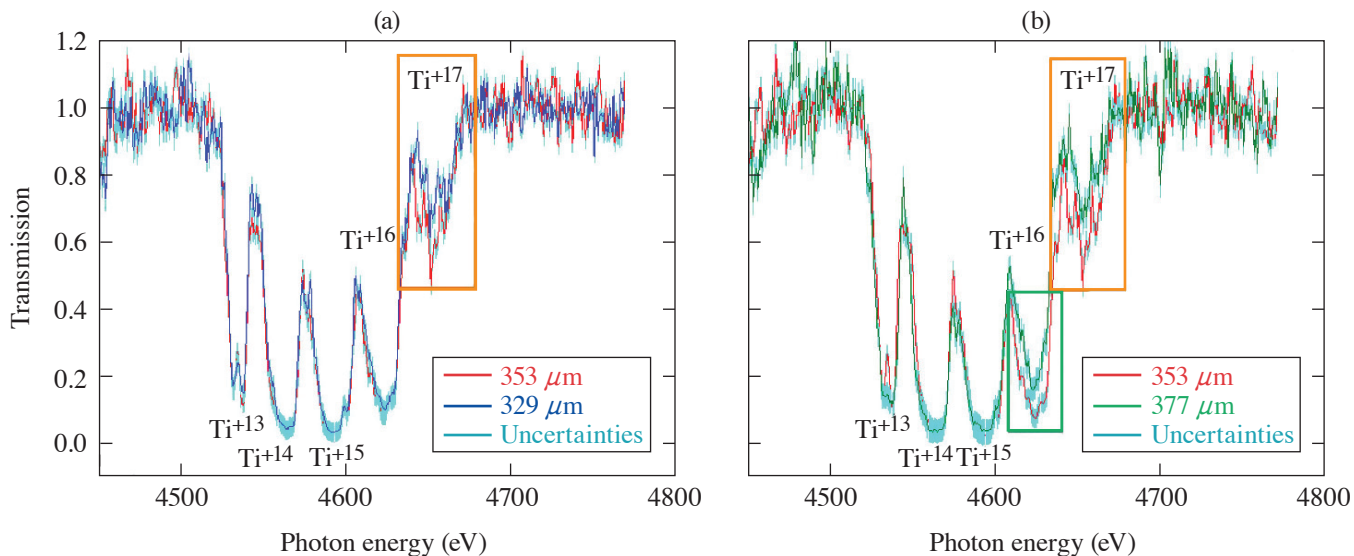
U2647JR

Figure 20
(a) Shot 90740 lineouts at 329 μm, 353 μm, and (b) 377 mm from the halfraum edge show increased absorption in Ti^{+17} at 353 μm, consistent with higher temperature. Reduced absorption in Ti^{+16} at 377 μm is consistent with lower temperature. This behavior signifies a temperature spike at 353 μm.

This work was performed under the auspices of the U.S. Department of Energy at Los Alamos National Laboratory under Contract No. 8923318CNA000001.

Discrete Vortex Model and ModCons Experiments

Principal Investigators: A. Rasmus, C. Di Stefano, K. Flippo, E. Merritt, F. Doss, N. Christiansen, A. Strickland, and D. Schmidt (LANL)

In FY20, the Discrete Vortex Model (DVM) and ModCons EP Campaigns did a combination of data collection and diagnostic development. DVM and ModCons used a shared experimental platform to study different aspects of hydrodynamic instability growth on interfaces. Three long-pulse beams were used to create a semi-sustained shock that drove instability growth. These campaigns utilized a Mn He$_\alpha$ (6.2-keV) backlighter in conjunction with the spherical crystal imager (SCI) or Fresnel zone plate (FZP) to create x-ray radiographs of interface evolution.

ModCons 20A measured the instability evolution of Richtmyer–Meshkov (RM), with delayed-onset Rayleigh–Taylor (RT), for a broadband perturbation. The experiments were built on data taken in FY19, using the same bulk platform, SCI diagnostic, and timings, but perturbation was used to seed instability growth. In particular, we kept the wavelengths in the perturbation the same but weighted the amplitudes so that either short or wavelength modes dominated (see Fig. 21). These data will inform models that use sub-grid models of instability evolution to initialize turbulence models.
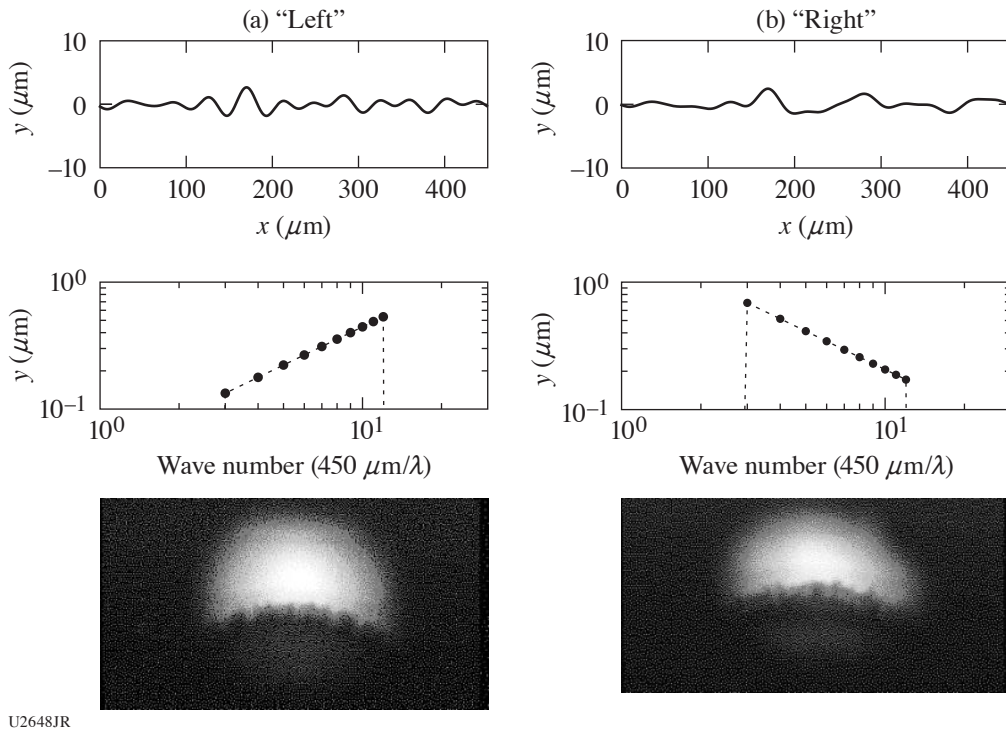
U2648JR

Figure 21
(a) The "left" and "right" perturbations which seeded instability growth in the ModCons 20A experiments. (b) Experimental radiographs showing the interface for each perturbation after 18 ns of instability evolution.

ModCons 20B used the same physics package as ModCons 20A but used the new FZP diagnostic instead of the SCI. The FZP diagnostic has the potential for greatly improved imaging resolution when compared to the SCI. We obtained a data set that will

allow us to think through the trade-offs between photon count, motion blur, and field of view for future ModCons experiments that use the FZP.

DVMEP 20A measured the evolution of a single strong point vortex quickly compared to the sound speed. This was achieved by shocking a single height discontinuity, or step, machined onto an interface. We successfully radiographed the point vortex evolution (see Fig. 22), and further analysis should yield insights into how the finite sound speed altered the flow surrounding the vortex.
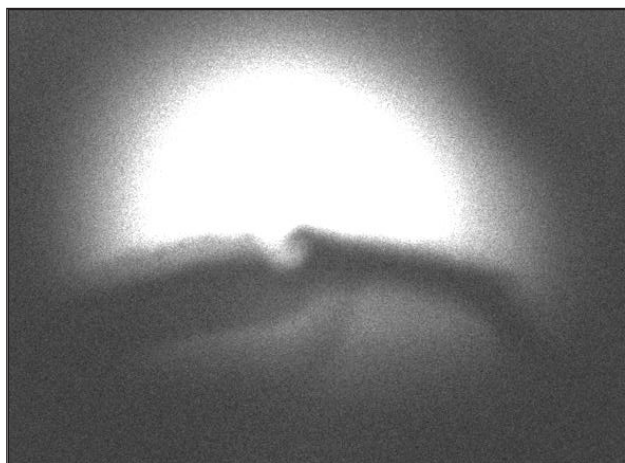

Figure 22
A radiograph of point vortex evolution taken in the DVM 20A experiments .

U2649JR

Observations of Dynamics of Void Collapse
Principal Investigators: P. M. Kozlowski, Y. Kim, B. M. Haines, A. Strickland, T. H. Day, L. Green, T. J. Murphy, and B. Albright

On 6 February 2020, the Marble team executed a series of experiments on OMEGA designed to understand how shocks interact with features such as voids. The goal of these experiment was to create a gas-filled void within a shock tube, similar to those encountered in Marble experiments on the NIF,[6,7] which would preheat and interact with a laser-driven shock. The Marble team made great improvements on a shock-tube design and was able to hold gas pressures up to 6 atm (Fig. 23). X-ray radiography diagnostics obtained data at 7-, 8.5-, 9.5-, 10.5-, and 11-ns delays after the shock drive, which enabled a study of the evolution
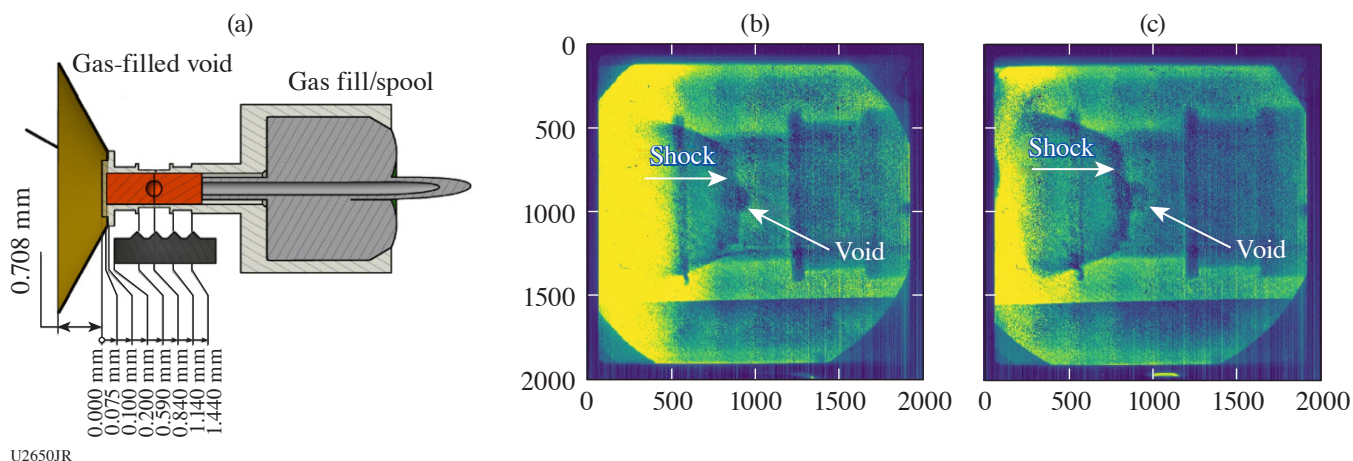

U2650JR

Figure 23
(a) An improved shock tube holding a gas pressure up to 6 atm. (b) A pure Kr-filled target (5.7 atm) taken 9.29 ns after the shock drive). (c) A mixture of Kr and H_2 target (5.6 atm) taken 9.31 ns after the shock drive.

of the gas-filled void. Throughout the shot day, we encountered a few technical issues such as losing two shot radiographs due to a charge-coupled–device (CCD) software issue (i.e., serial number issues on XRFC4), which forced the switch from CCD to film. In addition, a few shot radiographs voids were either not visible or difficult to see due to possible contrast issues. Despite such technical issues, the Marble team was able to compare dynamics with both pure krypton gas and a mixture of krypton and hydrogen gas fills to test how a void collapses and deforms under different plasma pressure conditions (Fig. 23). These experiments help us understand Marble experiments on the NIF as well as validate our computer models of the interaction of shocks in high-energy-density media with features.[8]

Evaluation of Two-Photon Polymerization Printed Structures as Low-Density Supports in Multi-Shell Targets

Principal Investigators: B. S. Scheiner, M. J. Schmitt, D. W. Schmidt, and L. Goodwin (LANL); and F. J. Marshall, P. M. Nilson, and R. S. Craxton (LLE)

The *Revolver* 20 A/B/C Campaigns evaluated the use of low-density (5- to 20-mg/cm^3) two-photon polymerization (2PP) printed structures as a support for the inner shell of a direct-drive double-shell target. The 2PP hemispherical structures, shown in Fig. 24(a), were printed in a stochastic lattice geometry and were composed of $CH_{1.72}N_{0.086}O_{0.37}$. From 1-D and 2-D simulations, it is expected that the lattices will disassemble by absorbing the radiation from the ablator's hot corona. The extent to which it can do so before bulk motion of the ablator depends on the lattice strut size and potentially on the lattices ability to absorb x-ray radiation. In experiments, the extent of the lattice disassembly is determined by measuring the perturbations imparted to the second shell, measured at a resolution of ~3 μm using the FZP imager. These experiments evaluated the performance of different lattice designs by varying the lattice strut size and average density and by adding a high-Z Au coating to assist in the absorption of x-ray radiation. Each lattice design is shown in Fig. 24(a). The corresponding FZP images are
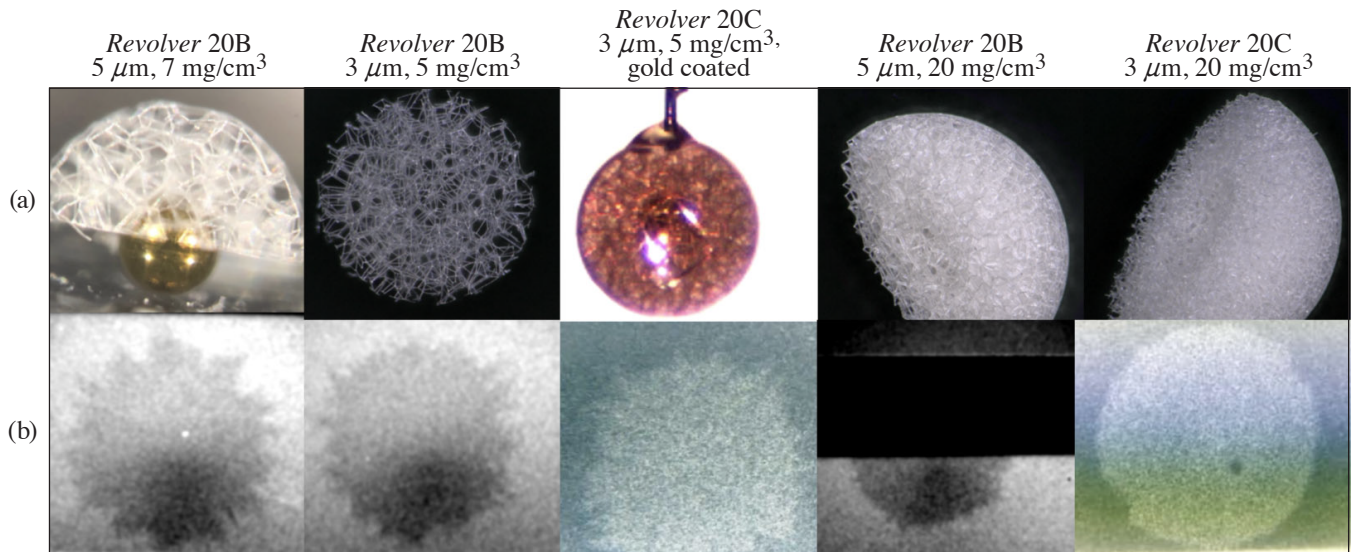
Figure 24
(a) The five different 2PP lattice designs used during the *Revolver* 20B/C shot days had differing lattice strut sizes and mass averaged densities. The first image shows a 2PP hemi attached to the Cr inner shell of the direct-drive double-shell targets. The center image shows the gold-coated lattice as viewed through the ablator of the assembled target. (b) The corresponding FZP image for each target type. The black bar in the fourth image is due to clipping by the edge of the framing camera strip.

shown in Fig. 24(b). While detailed analysis is underway, the general trend that is observed is that lattices with thinner struts result in a more-uniform inner shell for both ~5-mg/cm^3 and 20-mg/cm^3 lattices. The uniformity does not depend only on the strut size; an effect of the lattice void size is also at play. This effect is indicated by the superior uniformity of the 20-mg/cm^3 targets, regardless of strut size.

This research was supported by the Laboratory Directed Research and Development Program of Los Alamos National Laboratory under project number 20180051DR.

HEDB 20A High Energy Density with B Fields

Principal Investigators: K. A. Flippo, H. Li, Y.-C. Lu, S-.T. Li, A. Rasmus, C. Fiedler Kawaguchi,[*] and K. Kelso[*] (LANL); and D. Barnak (LLE)
[*]Also University of Michigan

The goals of this project were to test our understanding of a specific process in plasmas, namely self-generated magnetic fields, by creating them and measuring them experimentally in the laboratory, in conditions relevant to inertial confinement fusion (ICF) and high-energy-density (HED) physics. The design and modeling of the experiments were carried out mainly in *FLASH*, and *FLAG* was used for several comparisons of energy partition. In addition, hydro comparisons to *FLASH* were made using LANL's *xRAGE* to verify that the hydrodynamic behavior of *FLASH* was accurate for the resolutions used for 3-D simulations.

The existence of self-generated B fields in ICF plasmas has long been considered, but its impact has rarely been *quantified* in such environments. A popular misconception is that the likely B-field strength produces an energy density e_B that is small compared to the dominant energy density (often the thermal energy density e_{th} of the plasma) so that it is not "dynamically" important. But in reality, the self-generated and amplified (by turbulence) B fields need to affect only the turbulent energy density e_{turb} of the flow in order to dramatically impact how an experiment might evolve. Given the fact that e_{turb} can often be much smaller than e_{th}, B fields can indeed significantly affect the turbulence properties of ICF/HED plasmas without noticeably altering the overall global dynamics. For example, by altering the turbulence and mix evolution in the ICF implosion dynamics, the ignition performance can greatly degrade, as revealed by numerous NIF and OMEGA experiments.[9–14] Currently, B-field effects in ICF are typically not included and could be the reason simulations must alter the heat conduction by a factor of 2 to match ion temperatures.[9,14] Indeed, we have discovered another mechanism based on the concentration of ion species, which can play a role in ICF implosion that could be beneficial to hot-spot ignition. We have designed, executed, redesigned, and executed several experiments to get a meaningful measurement to quantify the self-generated fields and compare them with predictions using the latest ideas on plasma conductivity and extended magnetohydrodynamics (MHD).

This project used an extremely large amount of 3-D simulations to design our experimental platforms. This would not have been possible using the LANL advanced simulation and computing codes due to the time cost incurred in running these calculations. The reduced set of physics in the *FLASH* code, an adaptive mesh refinement Eularian code, allowed us to make use of the MHD in the *FLASH* code and the relatively good hydrodynamics (which were compared to *xRAGE* and many experiments) to carry out a large number of 2-D and 3-D simulations at 2- to 20-μm resolution.

In the end we tested two designs on the first shot day in 2019, which resulted in down-selecting to the counter-shear platform (Shock/Shear) with a modified internal layer to maximize B-field self-generation due to the so-called Biermann battery term found in extended MHD formulations. This is shown in Fig. 25(a). On the second shot day in 2019 we improved on the pRad diagnostic used to quantify the B field by adding a pepper-pot shield (PPS) to reduce the proton source to a pencil beam, which helped us find a simple shift in that source as a measurement of the B fields; the concept is shown in Fig. 25(b). That second 2019 day showed that we need to improve our signal levels of the proton source. The shot day in 2020 was the culmination of those improvements. Preliminary results are shown in Fig. 26. We significantly improved the signal level of the pRad source and are currently analyzing the collected data.
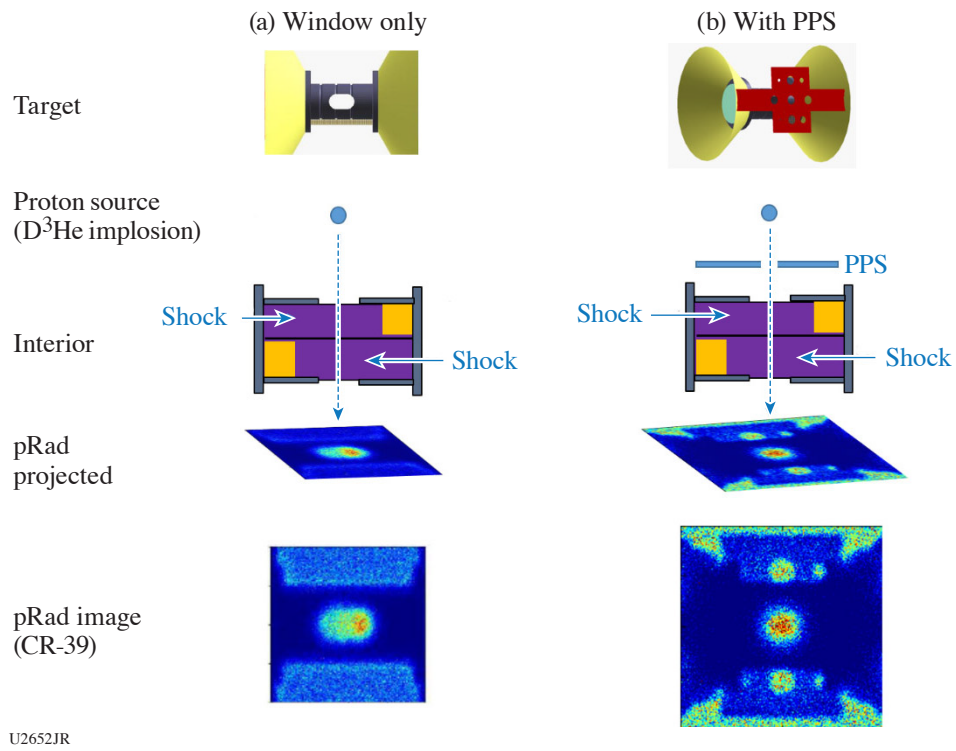
U2652JR

Figure 25
Setup of HEDB with (a) window only and (b) with the PPS showing the pRad axis and interior geometry and synthetic pRad images.
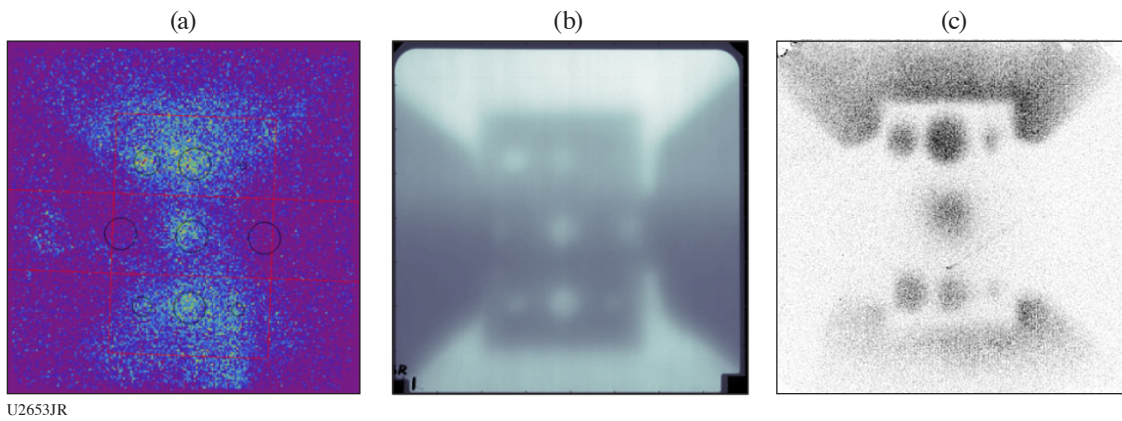
U2653JR

Figure 26
(a) pRad image from 2019 with (b) the accompanying x-ray image using the D^3He implosion as the x-ray source; (c) the improved signal-to-noise pRad from 2020.

MShock 2020

Principal Investigators: K. A. Flippo, F. W. Doss, C. Di Stefano, E. Merritt, and A. Rasmus (LANL)

The LANL HED Hydro team has adapted our OMEGA RM/RT instability platform to study the effects of heating on a shocked interface similar to what might occur in the inner shell of a double-shell–type ICF design. In our platform the interface can be heated before, after, or during shock and reshock using OMEGA and can easily be adapted and scaled to larger facilities such as the NIF as well. The current design allows for heating of one or two high-density interfaces separated by low-density foam. The material can be chosen with any density and/or composition typically 50 μm thick and can be heated from several eV up to around 100 eV, depending on material, thickness, and laser power. Strong shocks (from the drive beams) can then interact with these layers from either end of the shock tube. We are also testing the ability for the strongly heated layers to produce shocks themselves.

The platform is motivated by simulations presented in Haines *et al.*[15] The target design and laser setup are shown in Fig. 27. We use a point-projection backlighting (PPBL) scheme and the LANL CIPS tips on the cameras for imaging using vanadium, titanium, or chromium. The tube is a Be tube of 100-μm-thick walls and a 500-μm ID. The heaters are thin 10-μm-thick CH foils that span the two gold-cone shine-shields. Eight to nine beams can easily be used to heat the target before and during shock with the backlighter driver, which offers about 4 kJ of laser energy of which about 50% to 25% can be converted into hot electrons and x rays for heating the target.

On a previous shot day we measured the flux of hot electrons, which can extend to several hundred keV and are mainly responsible for the heating.[16] Of the 4 kJ, several hundred if not more can make it to the target to heat, depending on geometry. The data obtained on the last FY20 shot day show the heating of a 50-μm Ta layer expanding from heating to approximately 230 μm in width in 2 ns of time (see Fig. 28). Several issues affect the measurement of Ta since the layer is very opaque: just a small
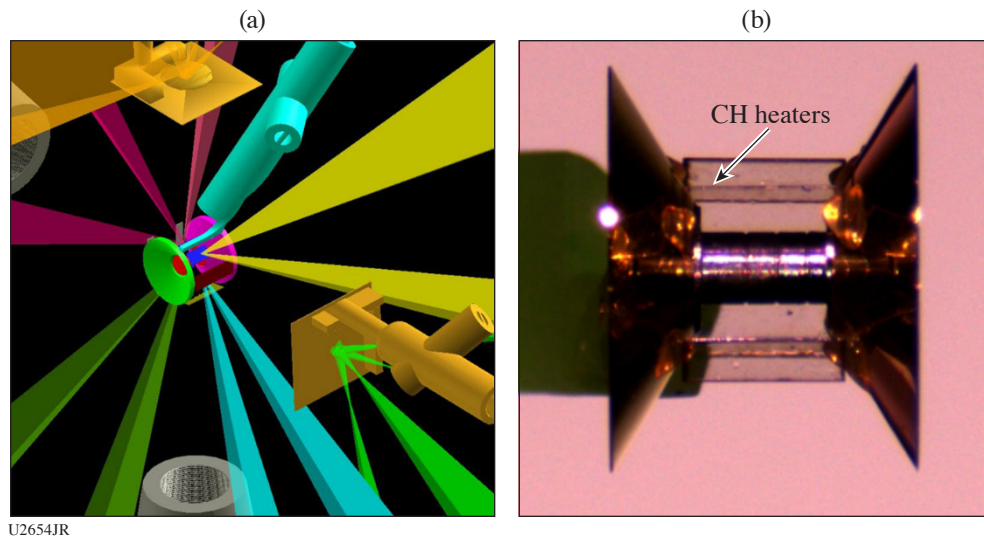

U2654JR

Figure 27
(a) The OMEGA heating setup with two orthogonal x-ray backlighters imaged via (b) PPBL and CIPS tips.
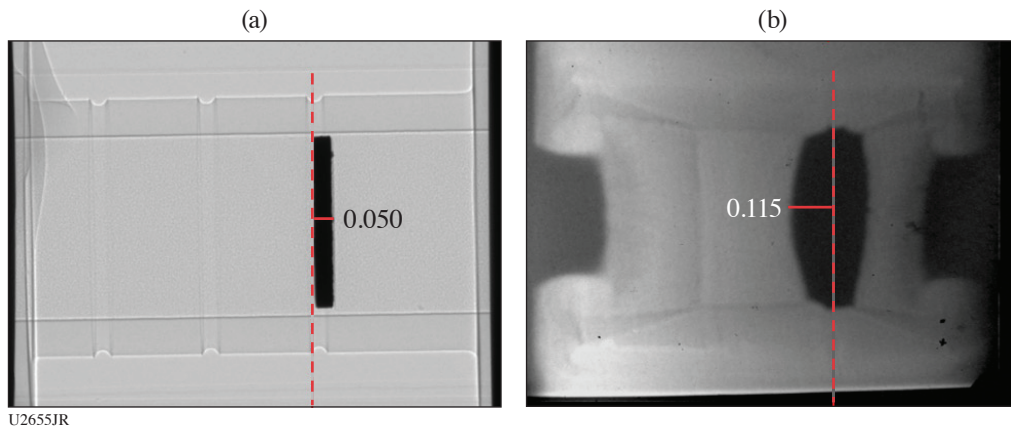
Figure 28
(a) Pre-shot radiograph and (b) heated, driven radiograph 2 ns after heating.

amount of material ablating off the surface can change the observed width. But if we assume it is the bulk material, it gives an upper bound of 1.3 keV in temperature, or 250 kJ of absorbed energy. The true temperature of the layer is certainly lower since the surface can absorb much lower energy radiation and heat preferentially. We are currently working on testing several materials to determine the strength of this effect.

REFERENCES

1. P. A. Bradley *et al.*, Phys. Plasmas **25**, 012710 (2018).

2. A. G. MacPhee *et al.*, Optica **7**, 129 (2020).

3. R. V. Shapovalov *et al.*, Phys. Rev. Accel. Beams **22**, 080401 (2019).

4. C. L. Fryer *et al.*, High Energy Density Phys. **35**, 100738 (2020).

5. H. M. Johns *et al.*, "A Temperature Pro File Diagnostic for Radiation Waves on OMEGA-60," to be published in High Energy Density Plasma Physics.

6. R. E. Olson *et al.*, Phys. Plasmas **27**, 102703 (2020).

7. T. J. Murphy *et al.*, J. Phys.: Conf. Ser. **717**, 012072 (2016).

8. B. M. Haines *et al.*, Nat. Commun. **11**, 544 (2020).

9. P. Tzeferacos *et al.*, Nat. Commun. **9**, 591 (2018).

10. J. Cao *et al.*, Phys. Plasmas **15**, 042102 (2008).

11. P. Y. Chang *et al.*, Phys. Rev. Lett. **107**, 035006 (2011).

12. H. Xu *et al.*, Astrophys. J. Lett. **698**, L14 (2009).

13. S. Li, Lawrence Livermore National Laboratory, Livermore, CA, Report LA-UR-03-8925 (2003).

14. S. Li *et al.*, "Implementation of Magneto-Hydrodynamic Solver for RAGE," Los Alamos National Laboratory, Los Alamos, NM (2007).

15. B. M. Haines *et al.*, Phys. Plasmas **20**, 022309 (2013).

16. T. R. Desjardins *et al.*, High Energy Density Phys. **39**, 100937 (2021).